JOURNAL OF AIRCRAFT
Vol. 54, No. 3, May–June 2017

Modifying Low-Drag Bodies to Generate Lift: A Computational Study

L. Smith,* K. J. Craig,† and J. P. Meyer‡
University of Pretoria, Pretoria 0002, South Africa
and
G. R. Spedding§
University of Southern California, Los Angeles, California 90089

DOI: 10.2514/1.C034051

Experimental work has shown that the flowfield around a wing-body configuration can be successfully modified with a short Kutta edge tail, so named because, by controlling the rear stagnation point, the circulation about the body can be effectively modified. The precise nature of the Kutta edge and body interaction were not considered, rather only the global flowfield effects. Therefore, the purpose of this study was to investigate the lift potential of low-drag bodies with Kutta edges, by numerically solving the flowfield around two low-drag bodies selected from literature. The drag and lift of the bodies were compared with experimental and numerical results in literature with good agreement. The geometries, computational grids, and boundary conditions of the two benchmark cases were then modified by adding short Kutta edges, for aftbody deflection angles of 2, 4, 6, and 8 deg at Reynolds numbers of 1.2×10^6 and 10^7. Both of the low-drag bodies showed similar average increases in lift and in pressure drag with the addition of the Kutta edge at increasing deflection angles. Though the configuration study is not yet complete, the results indicate a design space where there is potential for improvement in flight efficiency.

Nomenclature

A_m	=	body cross-sectional area at maximum diameter, m^2
AR	=	aspect ratio (Kutta edge width/Kutta edge length)
C_{DV}	=	volume-based drag coefficient
C_f	=	skin friction coefficient
C_L	=	lift coefficient
C_P	=	pressure coefficient
D	=	drag force, N
d	=	body diameter, m
L	=	lift force, N
l	=	body length, m
P	=	pressure, Pa
r	=	body radius, m
Re	=	$\rho U l/\mu$, Reynolds number
U	=	freestream velocity, m/s
U_x	=	streamwise velocity component, m/s
U_y	=	cross-stream velocity component, m/s
U_z	=	vertical velocity component, m/s
V_b	=	body volume, m^3
x	=	streamwise direction, m
y	=	vertical (wall-normal) direction, m
y^+	=	nondimensional wall distance
z	=	horizontal direction, m
δ	=	aftbody deflection angle, deg
μ	=	dynamic viscosity, kg/(m · s)
ρ	=	density, kg/m^3
τ_w	=	wall shear stress, Pa

Subscripts

F	=	F-57 low-drag body
f	=	friction component
L, α	=	lift slope at angle of attack
L, δ	=	lift slope at angle of deflection
M	=	Myring low-drag body
p	=	pressure component

I. Introduction

IN PRINCIPLE, a tail plane of an aircraft is unnecessary because static longitudinal stability can be achieved with variations in the main wing geometry alone [1]. Without this requirement, the long tubular body is neither necessary nor close to an optimum for either drag reduction or packing efficiency. If a different, shorter body is employed, it is possible to modify the flow around that body so that the circulation distribution between the body and the wings is much more uniform than with a tailplane. If that is so, both the induced drag and the total viscous drag can be reduced, owing to an improved body shape with a reduced wetted area.

Without the requirement for the long moment arm of a stabilizing tailplane, the fuselage design can consider a low-drag body (LDB) shape, which is typically shorter than traditional fuselage bodies. Various studies [2–13] have found, experimentally and computationally, that the optimum drag body would have a fineness ratio (length to maximum body diameter ratio) of between 4 and 6, which is significantly different from the current dominant passenger transport configuration (the so-called tube and wing) that uses a fineness ratio of 9 to 13. Most of the LDB studies considered the hydrodynamics of bodies or the low-speed (subsonic) aerodynamics of airship hulls.

Lift can be supported on an LDB simply by adding camber to the body of revolution. This strategy can, in principle, be combined with a trailing-edge tail/plate to yield quite significant performance benefits. In principle, if a tail contributes to the lift of an aircraft, it allows flight at a lower lift coefficient C_L of the main wing, further reducing the drag of the overall system.

For bodies of revolution, the boundary layer thickens over the aftbody, and as a result, there are substantial variations of pressure across the boundary layer leading into the near wake, characterized by strong viscous-inviscid interaction [6,14]. Added tail geometry now forms part of this aftbody and therefore will be influenced by not only the complex flows taking place in this region but also the potential

Received 31 May 2016; revision received 16 August 2016; accepted for publication 30 August 2016; published online 28 November 2016.

*Ph.D. Student, Department of Mechanical and Aeronautical Engineering; lelanie.smith@up.ac.za. Student Member AIAA (Corresponding Author).
†Professor, Department of Mechanical and Aeronautical Engineering; ken.craig@up.ac.za.
‡Professor, Department of Mechanical and Aeronautical Engineering; josua.meyer@up.ac.za. Member of AIAA.
§Professor, Department of Aerospace and Mechanical Engineering; geoff@usc.edu. Member AIAA.

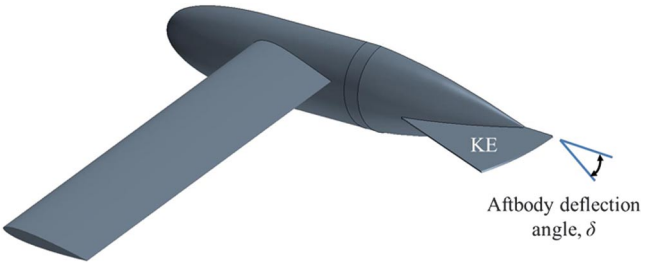

Fig. 1 Illustration of the wing-body-tail configuration with the KE and deflecting aftbody.

separation that can occur with low-drag bodies due to the adverse streamwise pressure gradient. If separation occurs, the tail would be situated in the viscous wake of the body, and the tail shape and size will no longer greatly influence the lift, because the Kutta condition will not be reached. Effective (increased L/D) body-tail interaction would depend on the flow remaining attached over the aftbody and the tail.

Huyssen et al. [15] and Davis and Spedding [16] showed experimentally that the trailing edge of a fuselage can be used to control circulation in the central region of the aircraft, in support of the original notion that the primary role of the Kutta edge (KE) was to enforce a particular location of the aft stagnation point. The KE appeared to modify the global flow around the body so that the circulation distribution between the body and the wings was more uniform, which, in principle, leads to a reduction in induced (inviscid) drag. However, the argument was only indirectly supported by the findings of modified downwash profiles in the near wake, and the mechanism by which the global flowfield was changed could not be directly identified, either from particle image velocimetry (PIV) in the wake [15,16] or with global force balance measurements [16]. We note also that no attempt was made to optimize the wing-body-tail configuration, and both studies used a simple geometric form for the shorter body (not an LDB) and with a discrete KE, which was not blended or integrated to the body shape. The KE itself was also fixed to the conical aftbody, so that KE deflection was always linked with deflection of the aftbody. The deflection was described by a single angle δ, shown in Fig. 1, of the wing-body-tail configuration.

The force balance and PIV measurements [16] showed that the lift experienced by the aircraft with a KE increased with δ up to a certain maximum. The aftbody deflection makes a positive camber of the body and thus potentially a nonzero circulation over it. The addition of the KE achieved the same effect at a lower δ and contributed to lift as δ increased. It was concluded that the most effective means of generating asymmetry and net lift on a body was through deflection of the KE.

The purpose of this study is to more thoroughly investigate the potential of a KE to modify the flow over LDBs. A numerical investigation of two LDBs selected from the literature was conducted, and the geometries were then modified with a KE attachment. Forces and flowfields with and without a KE (which we subsequently term KE and NKE conditions) at varying δ were computed to determine the mechanism of the KE/body deflection on both local and global lift and drag, computed from the normal and shear stresses over the whole body assemblage.

II. Numerical Modeling

A. Geometric Model and Mesh Generation

The two LDB geometries were the F-57 body from Parsons and Goodson [6] and the body of revolution from Myring [8]. In both papers, equations were given that describe the outer geometry of the bodies, and these were used to generate the scalable body profiles. The F-57 LDB was selected because data (pressure distribution, mean velocity distribution, and Reynolds stresses) were published by Patel and Lee [9] for the same geometry in wind tunnel experiments; the Myring LDB was used because theoretical velocity distribution results were available [8].

Both bodies were modeled as three-dimensional axisymmetric bodies inside a three-dimensional computational flow domain

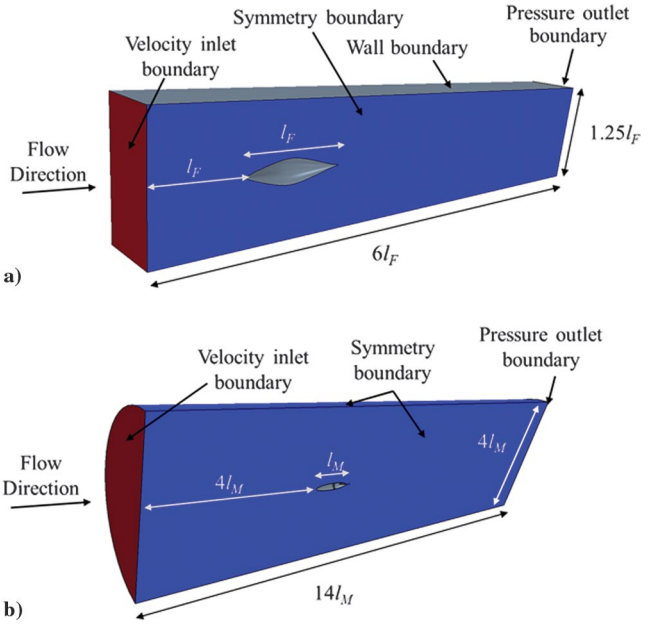

Fig. 2 Geometric model and the assigned boundary conditions for a) the F-57 LDB, and b) the Myring LDB.

(Fig. 2). Three-dimensional (not axisymmetric) grids were necessary so as to accommodate the later addition of symmetry-breaking KE tails. The simulation of the wind tunnel experiments (for the F-57) includes an approximation of the wind tunnel walls, which were originally in octagonal cross section [9] but simplified to a square cross section here (with less than 0.5% influence on the force coefficient results). The fineness ratio of the body was 4.75, the height and width of the wind tunnel were $1.25l_F$, and the test section length was $6l_F$ as in the experimental investigation [9].

The Myring LDB, with body length l_M and fineness ratio 5.55, was modeled inside a cylindrical domain with diameter $4l_M$. The nose of the body was positioned $4l_M$ from the inlet of the grid, and the outlet was $9l_M$ downstream of the tail.

The computational grids (Fig. 3) consisted of polyhedral cells and were meshed using the Advancing Layer Mesher in Star-CCM+ [17]. This mesh function enabled the mesh to grow around sharp corners on the body without collapsing. The growth of the boundary layer along the body and KE starts with a very thin boundary layer over the nose, gradually thickening toward the trailing edge. Both LDBs had 20 cells across the boundary layer height for improved drag estimation, whereas two boundary layer cells were sufficient for the simulated tunnel walls.

Three volumetric mesh refinements were used for the two LDB grids. The first and second drove the cells to be finer around the bodies and to gradually increase the cell size away from the bodies, whereas the third drove the sections at the trailing edge and wake regions to be finer. Primarily, these refinements increased the mesh density where viscous effects were expected to be more prevalent. Additional refinements were applied at the streamwise location on the F-57 LDB where transition was experimentally forced with a tripwire [9] ($x/l = 0.475$) as well as for the nose and tail sections on both bodies.

To assure mesh independence, the grid-convergence index method [18] was used on the three different mesh sizes of each grid. The final mesh counts for the F-57 and Myring LDB (with no KE) were about 3.6×10^6 and 3.3×10^6 cells, respectively.

The KE tails had the same geometry as described in [15,16], with the same ratios of tail width to body diameter and KE length to the total body length. The addition of the KE tails increased the body lengths by 10%, but it proved unnecessary to extend the domain length correspondingly. The KE tails increased the cell counts to 4.6×10^6 and 3.4×10^6 for the F-57 and Myring bodies, respectively. Similar mesh independence studies were conducted on these domains as with the two reference cases.

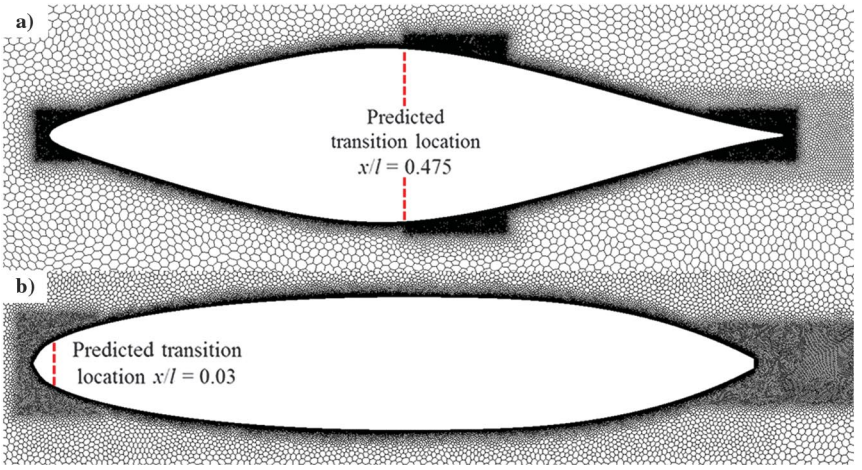

Fig. 3 Unstructured meshes around a) the axisymmetric F-57 LDB, and b) Myring's LDB. Predicted transition location are indicated.

B. Boundary Conditions, Turbulence, and Transition Models

The boundary conditions used for the simulations are indicated in Fig. 2. The flow was assumed to be steady and incompressible, with a constant-velocity inlet condition. Reynolds numbers based on body length were 1.2×10^6 for the F-57 LDB and 10^7 for the Myring LDB. The outlet boundaries were pressure boundaries set at atmospheric conditions. The F-57 LDB's outer surface domains were modeled as no-slip wall boundaries, where the outer boundaries for Myring's LDB had symmetry boundaries. The nondimensional wall distance criterion $y^+ < 1$ was satisfied for all cases (the predicted wall boundary thicknesses are less than a wall-bounding computational cell, and the boundary layer can therefore be modeled on that cell). The inlet velocity was specified to give the Reynolds numbers at which the literature/reference cases were completed.

The Star-CCM+ solver for the Reynolds-averaged Navier–Stokes (RANS) equations with the shear-stress transport (SST) k-ω turbulence model [19] was used in all cases. Although details of the turbulent fluctuations are not required to model global lift, drag is more sensitive to these details. The SST k–ω turbulence model was selected because it has successfully been used in predicting onset of flow separation [20]. In both LDBs, there is the possibility of laminar separation over the aftbody, when a transition model is important to accurately estimate the force coefficients. The γ–Re_θ transition model [21] was used to predict laminar-turbulent transition.

III. Comparison with Reference Cases

A. F-57 Low-Drag Body

Figure 4a shows the numerically generated pressure coefficients C_P over the F-57 in the normalized axial direction x/l, together with

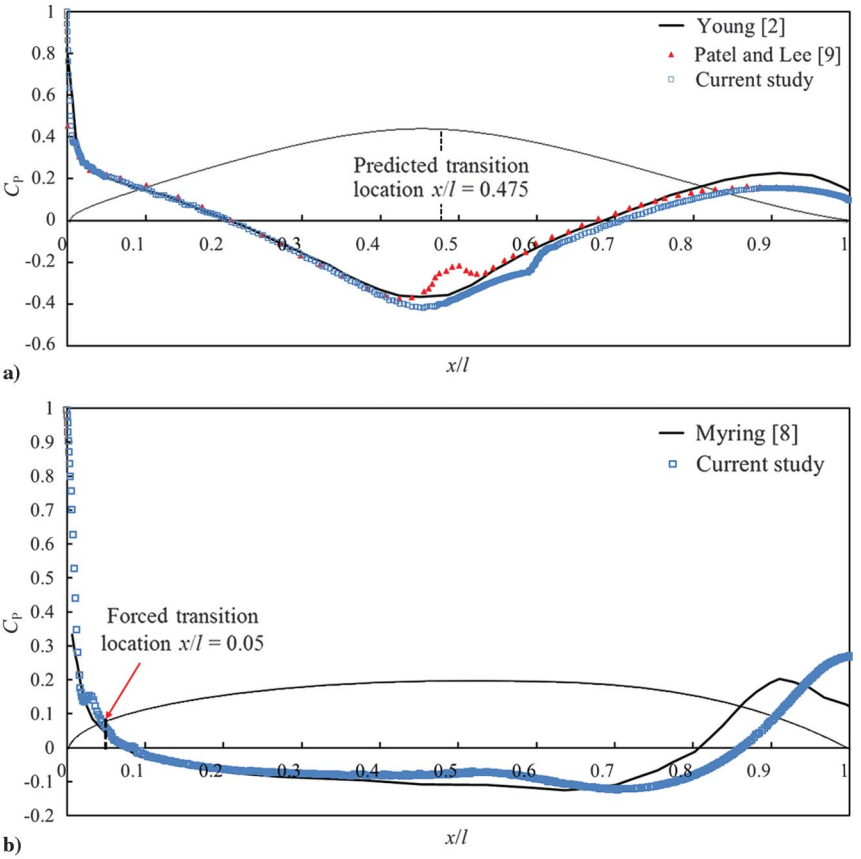

Fig. 4 Pressure coefficients for a) F-57 LDB at $Re = 1.2 \times 10^6$, and b) the Myring LDB at $Re = 1 \times 10^7$, comparing the simulations to literature results [2,8,9].

the experimental results of Patel and Lee [9] at $Re = 1.2 \times 10^6$ and the theoretical predictions from Young [2]. Young made use of a modified airfoil method to predict profile drag for smooth bodies of revolution, though he found that this method has some restrictions. At higher Reynolds numbers (10^7–10^8) and low fineness ratio (3.25–5.9), where the transition region did not exceed $x/l = 0.05$, the method gives reasonable results compared with experimental cases. However, when both Reynolds number and l/d are lower, the assumption of negligible pressure variation in the boundary layer on the aftbody is not correct because the thickening boundary layer can support substantial pressure variation [6,9].

There are negligible differences between theory, experiment, and simulation (less than 7%) up to $x/l = 0.4$. Further aft, close agreement cannot be expected because the experiments were conducted with a tripwire at $x/l = 0.475$ to avoid a separation bubble. The numerical departure in C_P at about $x/l = 0.57$ shows the location of the natural separation bubble absent a tripwire. From $x/l = 0.7$, the wind tunnel and simulation results agree well and depart from the high C_P theoretical line, likely due to finite Reynolds-number effects, as noted previously.

B. Myring's Low-Drag Body

Figure 4b compares the pressure coefficients with theoretical predictions of Myring [8] for $Re = 10^7$. The overall agreement is reasonable for $x/l < 0.4$. Theory and computation differ downstream of this point because numerical results show an initial reduction in $-C_P$ before it recovers to a positive tail toward the trailing edge. Consequently, theory and numerical values have a difference in phase in the undulation in $C_P(x)$. Analogous to the previous F-57 case, Myring [8] prescribed a transition location at $x/l = 0.05$ where the numerical simulation allows transition to occur naturally at approximately $x/l = 0.48$, which is partially the cause for the difference in phase seen in Fig. 4b.

IV. Aerodynamic Effect of Deflected Tail Plates on Low-Drag Bodies

A. F-57 Low-Drag Body with Kutta Edge Tail

The pressure distributions along the F-57 LDB for both the KE/NKE conditions at varying aftbody deflection angles δ are shown in Fig. 5a. All the cases are similar over the nose and up to $x/l = 0.57$, after which a separation bubble occurs up to approximately $x/l = 0.6$. This separation bubble is shown in Fig. 5b with the wall shear stress τ_w over a section of the body ($0.55 < x/l < 0.62$) where a recirculation zone occurs inside a separation bubble for both KE and NKE at $\delta = 0$ deg. The details of the bubble geometry are sensitive to the numerical stability of the transition model and the prescribed turbulence intensity, but its existence is not unreasonable.

The aftbody deflection point is at $x/l = 0.63$ in Fig. 5a. Immediately after, dP/dx is strongly positive, and C_P changes sign at about $x/l = 0.72$. For NKE, dP/dx increases with increasing δ. The peak amplitude of positive C_P is much higher for NKE than KE and when $\delta = 8$ deg; the KE case has a very shallow plateau. The KE starts at $x/l = 0.77$, where it is immediately associated with a reduction in C_P (relative to NKE), and the maximum positive C_P is found farther downstream.

Figure 6 shows the normalized streamwise wake velocity profile U_x/U for $\delta = 4$ deg with and without a KE. The profiles are taken at $x/l = 1.005$ for NKE and $x/l = 1.105$ for KE (0.5% after either the body or KE ends). The downward deflection of the defect profile with KE implies a higher lift, and the color inset of velocity contours shows that the displacement is a global field phenomenon.

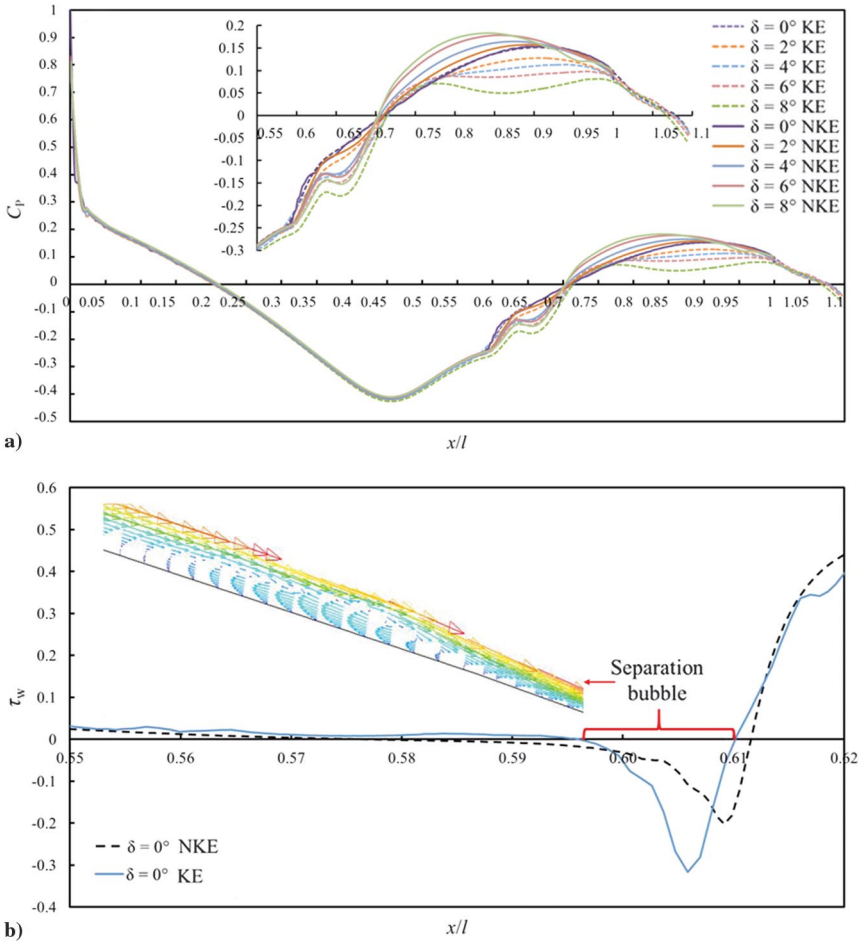

Fig. 5 a) Pressure coefficient of the F-57 LDB-NKE/KE at different δ, and b) wall shear stress over the section of the body $0.55 < x/l < 0.62$ with and without the KE.

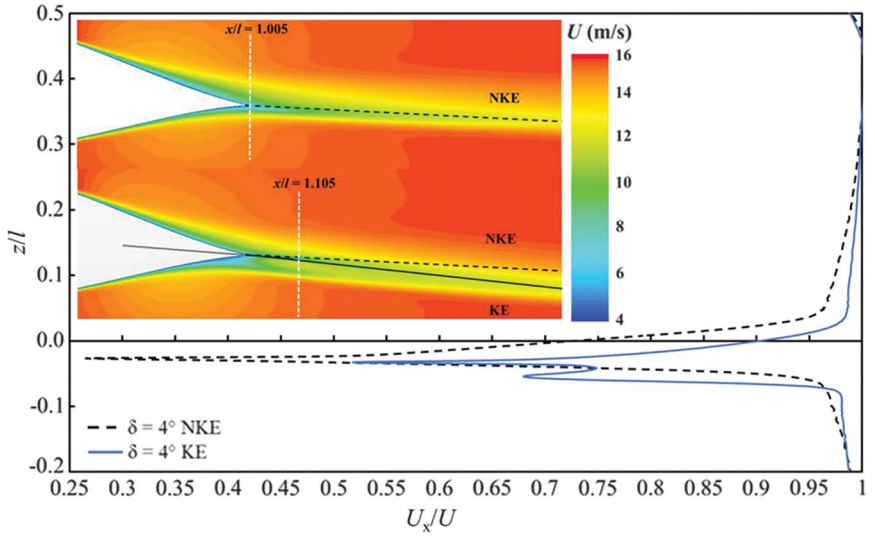

Fig. 6 Normalized streamwise wake velocity profile for the F-57 LDB-NKE/KE. Insert shows velocity magnitude contours on the symmetry plane in the wake region.

Figures 7a and 7b show U_x/U for $\delta = 2$ and 6 deg, combined with contours of the relative vertical velocity U_z/U at the symmetry plane of the body with and without a KE. Similar to [16], the U_x/U profile has a double-lobe form, as though upper and lower boundary layers were shed separately into the wake with the KE, which acts like a splitter plate. The lower lobe becomes more pronounced as δ increases. The flow around the LDB-KE shows a larger vertical deflection over the aftbody than the equivalent NKE. The boundary layer over the aftbody top and bottom is split by the KE, which prevents the formation of a proximate mixing zone between these two shear layers. In the absence of the KE, the presence of a pressure differential between the upper (low-pressure) and lower (high-pressure) surface of the body leads to an upward and swirling flow around the aftbody side as indicated in Fig. 8 ($\delta = 4$ deg at $x/l = 1.005$). The addition of the KE blocks the upward flow on the body of the LDB, and the pressure difference now drives the flow to form a tip vortex on the outer edge of the KE. The blockage of the LDB onbody vortex formation and consequent transverse flow around the KE forms the double-lobe in the velocity profile (Fig. 7).

To evaluate and compare aerodynamic force coefficients of the LDB-KE combinations, the reference areas were selected as follows. At any given fineness ratio, the maximum diameter area-based drag coefficient depends on the body geometry, and so the drag coefficient is written as

$$C_{\mathrm{DV}} = \frac{D}{(1/2)\rho U^2 V_b^{2/3}} \tag{1}$$

where V_b is the volume, ρ is the density, U is the freestream velocity, and D is the drag force.

Figure 9a shows that neither the pressure $C_{\mathrm{DV},p}$ nor the friction $C_{\mathrm{DV},f}$ components of C_{DV} for the F-57-NKE vary significantly with δ. However, with KE, $C_{\mathrm{DV},p}$ increases by almost a factor of 4 from $\delta = 0$ deg to $\delta = 8$ deg. This $C_{\mathrm{DV},p}$ increase is due to the increase of the effective base area when the KE deflects downward, indicated by the schematic inset of Fig. 9a.

The body lift depends on the displacement of streamlines over the body, and so the appropriate reference area is the area at the maximum body diameter, A_m, and C_L is defined as

$$C_L = \frac{L}{(1/2)\rho U^2 A_m} \tag{2}$$

In Fig. 9b, C_L is shown as function of δ for the F-57 body, with and without KE. Without the KE, the maximum increase in C_L based on frontal area is only 3% for the largest $\delta = 8$ deg. With KE, C_L for the body-tail combination increases almost linearly with δ. One can define an average lift slope $\Delta C_L/\Delta\delta = C_{L,\delta} = 0.3/4/\,\mathrm{deg}$ or $4.3/\mathrm{rad}$. The lift slope $C_{l,\alpha}$ of a three-dimensional delta wing is AR $\pi/2$, and if we set AR for the KE tail to be about 1, the expected lift slope is therefore $\pi/2 = 1.6/\mathrm{rad}$. The fact that $C_{L,\delta}$ is approximately 2.7 times this value indirectly argues for the effect of the tail being nonlocal, increasing lift on the whole body.

Figure 10 shows the vertical velocity component U_z/U as a function of spanwise normalized body radius y/r, with and without a KE for $\delta = 0$–4 deg (Fig. 10a) and $\delta = 6$ and 8 deg (Fig. 10b). These profiles are taken at $z/r = 0.7$ above the wake and at streamwise location $x/l = 1.005$ (NKE) and $x/l = 1.105$ (KE). The maximum body diameter is at $y/r = 1$, and the KE ends at approximately $y/r = 1.45$. The downwash profiles at $\delta = 0$ deg (Fig. 10a) are indistinguishable for NKE and KE, as one might expect. As δ increases to 4 deg, the KE leaves a much stronger and broader downwash signature. With further increases in δ (Fig. 10b), though the centerline value of U_z may be similar between KE and NKE, the spanwise region influenced is more extensive in the KE condition. The KE case at high δ is associated with significant upwash for $y/r > 1.1$, and the net integrated downwash increment (and hence lift) might be expected to be smaller, based on this observation alone. We may again infer that the lift is determined in large part by the global influence of deflected streamlines over the entire body, and not just localized at the tail.

B. Myring's Low-Drag Body with Kutta Edge Tail

Figure 11 shows the pressure distribution over the Myring LDB for NKE/KE cases at varying δ. The Myring LDB (at the higher Reynolds number) does not have a prominent separation bubble (unlike the F-57 LDB). There is, however, a brief and abrupt pressure drop as the flow accelerates over the aftbody deflection point at $x/l = 0.63$. After this point, the KE curves are all lower than the NKE cases for much of $x/l > 0.7$ (as they also were for the F-57 in Fig. 5a).

Figure 12 shows U_x/U for KE/NKE for $\delta = 4$ deg on a Myring LDB. The downward deflection of the peak in the defect profile with KE is greater than that of the F-57 LDB (cf. Fig. 6). The characteristic double-lobe profile is also less pronounced.

Figures 13a and 13b show that the KE condition is always associated with greater deflection of the U_x/U profiles, which are nonetheless weaker than the NKE equivalents. Again, the addition of the KE leads to a transverse flow over the aftbody to produce the double-lobe velocity profile as with the F-57 LDB. However, the double-lobe is less pronounced for the Myring LDB, a fact that can be traced back to differences in boundary layer development across the aftbody. The Myring LDB was designed with a

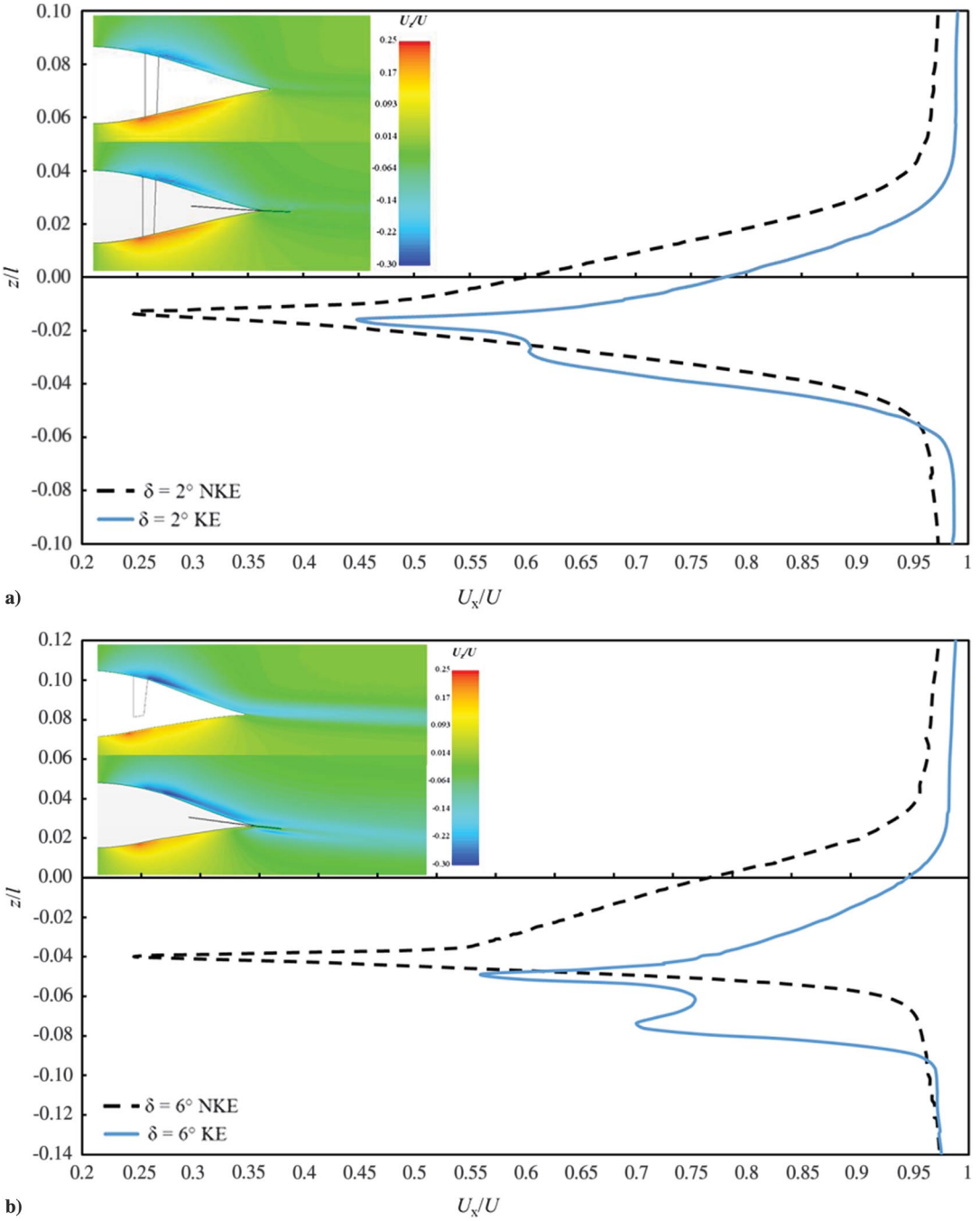

Fig. 7 U_x/U of a) $\delta = 2$ deg, and b) $\delta = 6$ deg, for the F-57 LDB-NKE/KE. Inserts show relative velocity magnitude contours on the symmetry plane in the wake region.

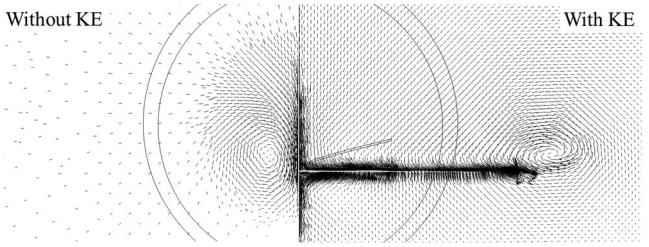

Fig. 8 Velocity vectors at $x/l = 1.005$ for F-57 LDB at $\delta = 4$ deg with (right) and without (left) KE.

combination of delay of transition and reduction of adverse pressure over the aftbody, without large amplitude streamwise variation in pressure (Figs. 4a and 4b). The F-57 LDB was designed only on the condition for delayed transition. The differences in aftbody design criteria lead to differing boundary layer conditions at the LDB-KE interface. Figure 14 shows the profiles of the top and bottom surface boundary layers for the two LDBs with and without the KE, with inserts of velocity vector profiles through the boundary layers over the aft bodies at $x/l = 0.99$. The boundary layer for the F-57 LDB-KE has a steeper $\mathrm{d}U/\mathrm{d}z$ than the Myring LDB-KE because of the sharper taper aftbody geometry and more gradual pressure recovery (Figs. 4a and 4b). Figure 15 shows that ΔP for the Myring LDB-KE from $y/r = 0$ to 6 is about twice that of the F-57 LDB-KE under the same conditions. The Myring LDB has a better interaction with the KE owing to the more bluff aftbody geometry and gradual pressure recovery as well as the attendant less pronounced double-lobe wake profile (Fig. 14).

Figure 16a shows $C_{\mathrm{DV},f,p}(\delta)$ for the two NKE/KE configurations. According to Myring [8], the skin friction drag contributes 90% of the

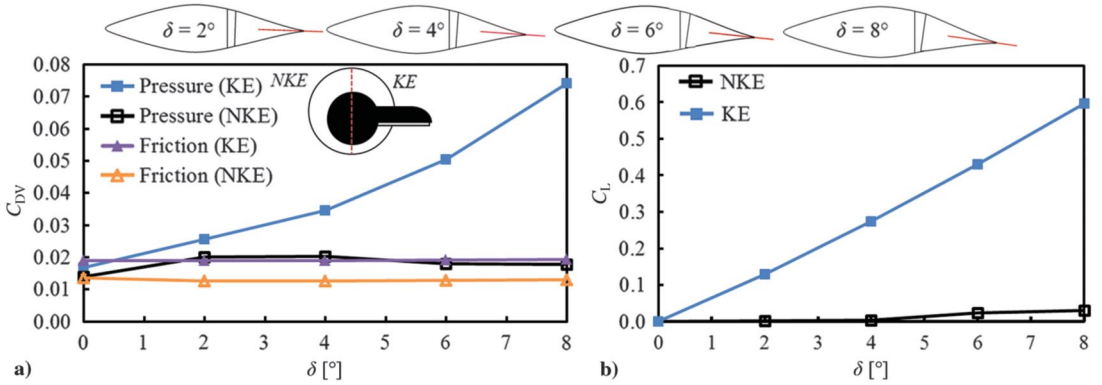

Fig. 9 Volume-based drag components of a) pressure and friction, and b) lift coefficients, for the F-57 LDB-NKE/KE at different δ. Insert illustrates the effective base area for the NKE and KE.

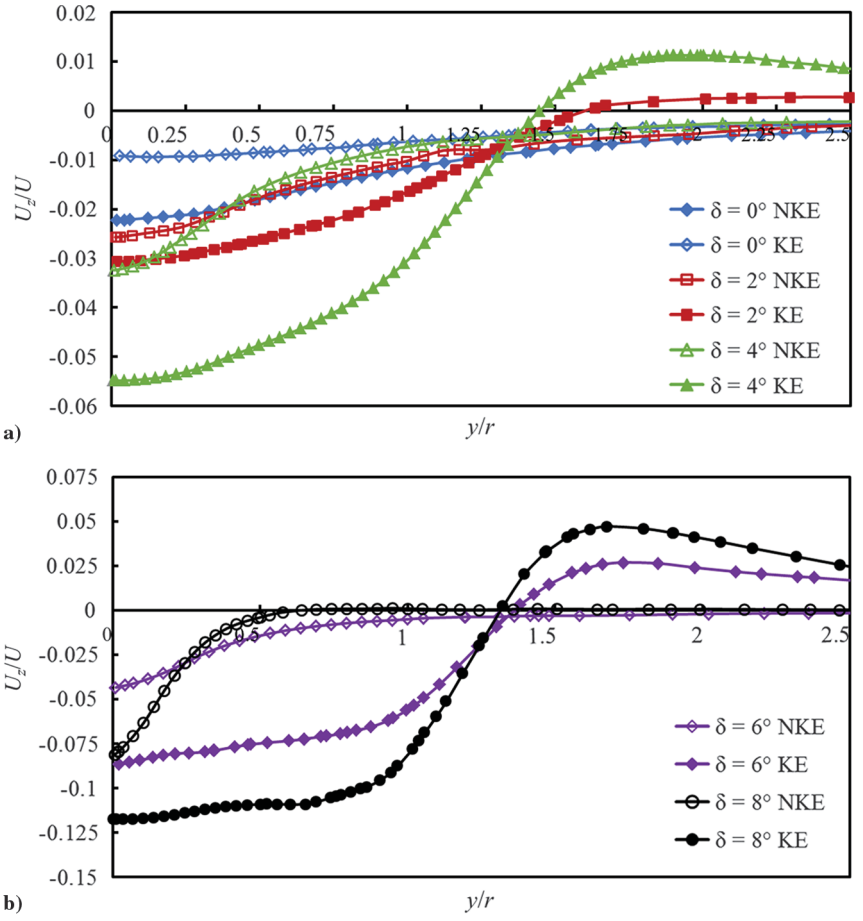

Fig. 10 U_z/U as a function of y/r, for the F-57 LDB: a) $\delta = 0$–4 deg, and b) $\delta = 6$ and 8 deg.

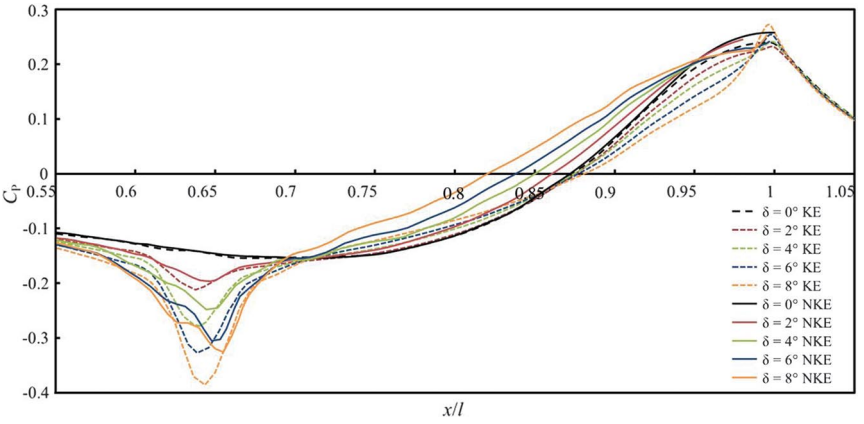

Fig. 11 Pressure coefficient as a function of dimensionless body length of the Myring LDB-NKE/KE at different δ.

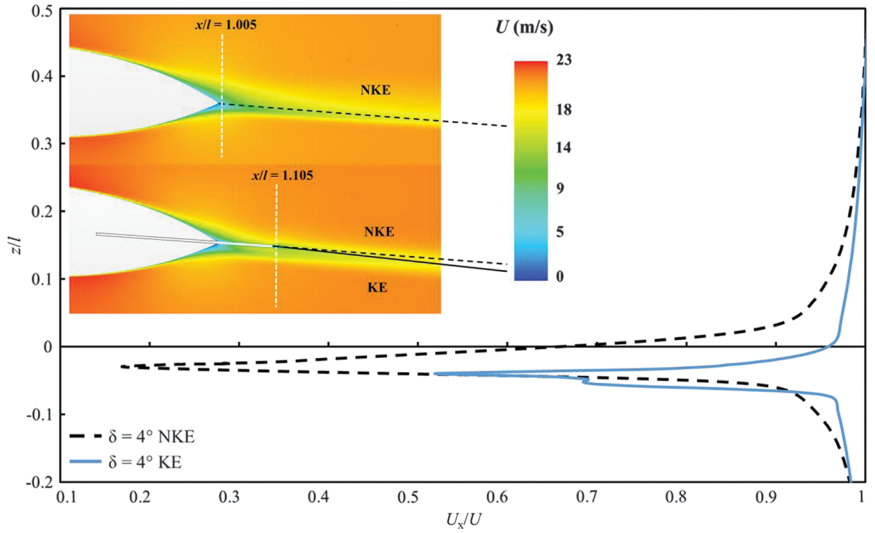

Fig. 12 Normalized streamwise wake velocity profile at $\delta = 4$ deg for the Myring LDB-NKE/KE. Insert shows velocity magnitude contours on the symmetry plane in the wake region.

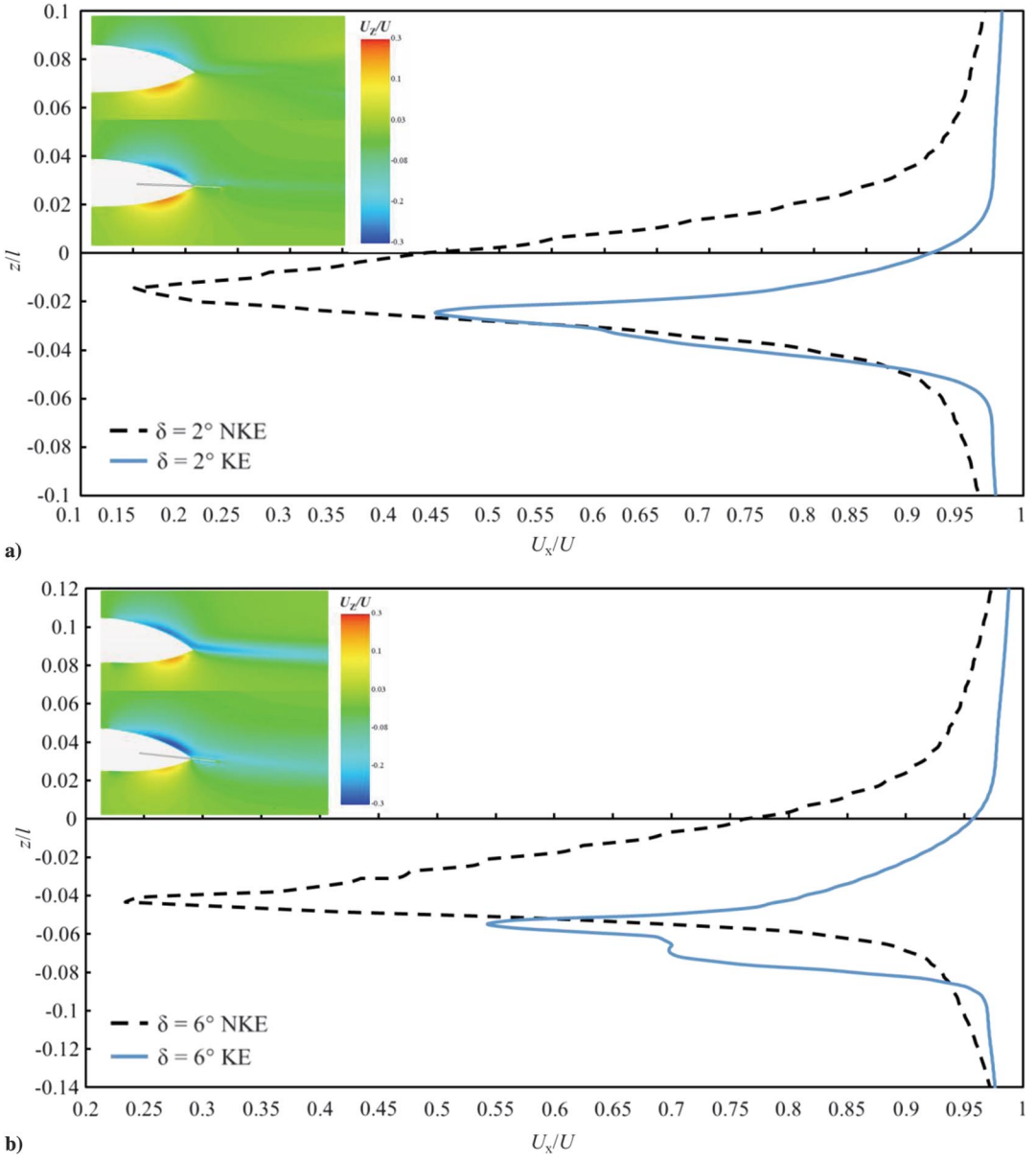

Fig. 13 U_x/U of a) $\delta = 2$ deg, and b) $\delta = 6$ deg, for the Myring LDB-NKE/KE. Inserts show relative velocity magnitude contours on the symmetry plane in the wake region.

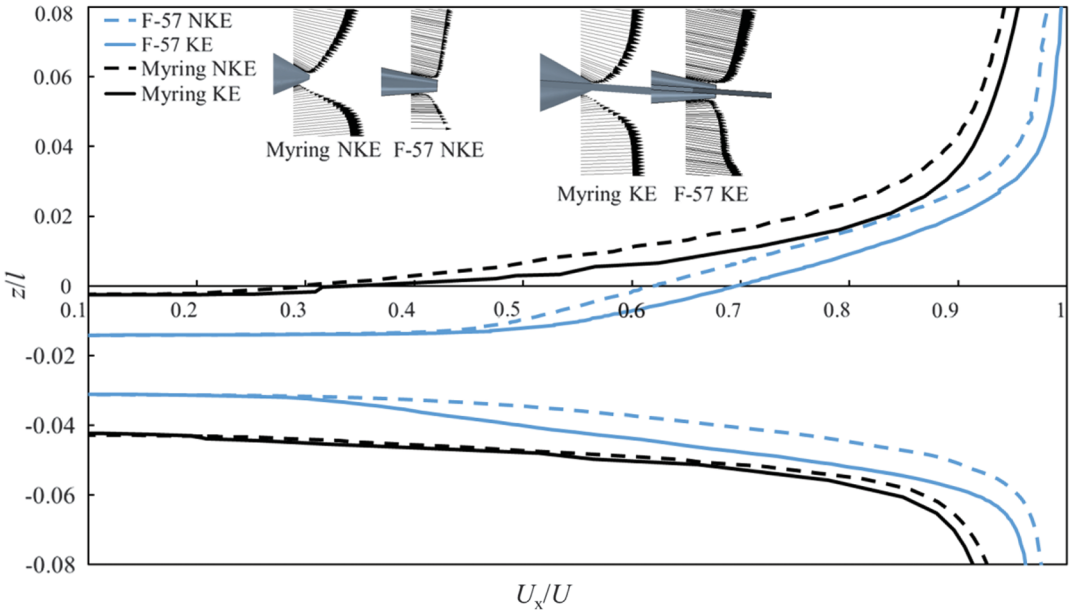

Fig. 14 Profiles of the top and bottom surface boundary layers for the two LDB-NKE/KEs at $\delta = 4$ deg.

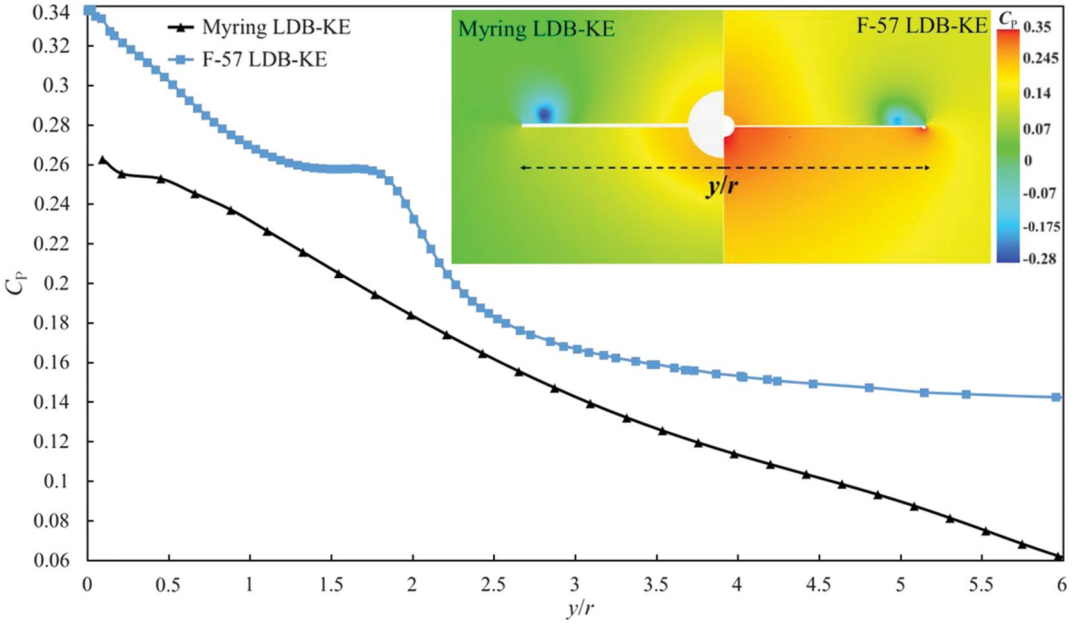

Fig. 15 Pressure coefficients at $x/l = 0.96$ for the F-57 and Myring LDB-KE at $\delta = 4$ deg. Insert of pressure contours on the cross-stream plane at $x/l = 0.96$.

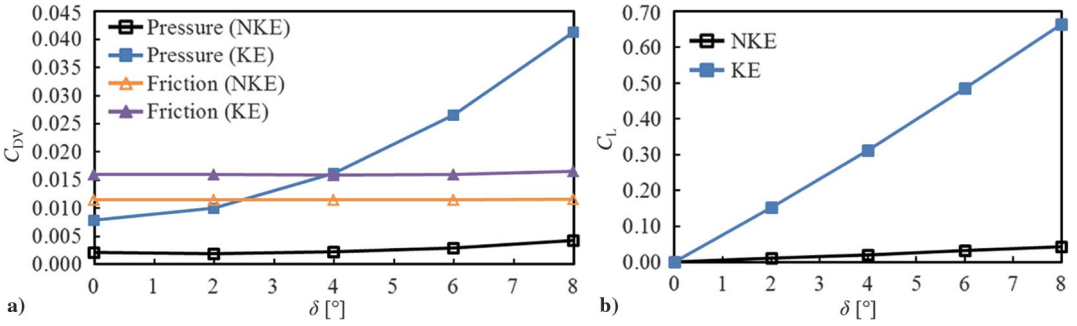

Fig. 16 Volume-based drag components of a) pressure and friction, and b) lift coefficients, for the Myring LDB-NKE/KE at different δ.

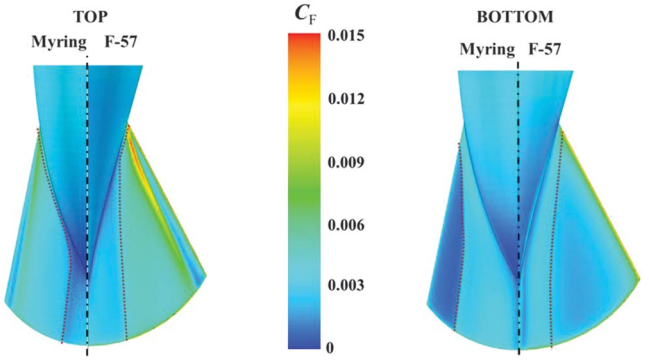

Fig. 17 C_f **the top and bottom surface of the KE for the F-57 and Myring LDB-KE at** $\delta = 4$ **deg. Dashed lines show the wake edge on the body surface.**

total drag experienced by the unmodified body, and Fig. 16a for the NKE case at $\delta = 0$ deg does show that the $C_{DV,f}$ is approximately 85% of C_{DV}. The Myring LDB and F-57 LDB show similar, and quite large, increases in $C_{DV,f}$ when the KE is added, with little sensitivity to increasing δ. The $C_{DV,p}$ for the Myring LDB-KE at $\delta = 0$ deg initially contributes to 33% of the C_{DV} and becomes the leading contribution to C_{DV} after $\delta = 4$ deg. By contrast, $C_{DV,p}$ previously shown for the F-57 LDB-KE in Fig. 9a initially contributes 45% of the total at $\delta = 0$ deg but then has a sharper increase with δ, rising to $C_{DV} = 0.07$ at $\delta = 8$ deg, compared with about 0.04 here for the Myring LDB.

The Myring LDB also has a steep increase of C_L with δ (Fig. 16b), with a mean lift slope $C_{L,\delta} = 4.8/\text{rad}$, which is higher than for the F-57 LDB and now three times the lift slope for an AR = 1 slender wing. In summary, the Myring LDB has a larger increase in C_L but a smaller increase in C_{DV}, with increasing δ, for the KE case. The reasons may be traced to the different environments in which the KE is immersed, which come from the differing design emphases.

The different conditions can be seen in the contours of skin friction distribution on the upper and lower KE surfaces for the two bodies (Fig. 17). If one sets a threshold C_f at the expected flat plate boundary layer value for the inlet conditions onto the KE for both, then a central wake can be distinguished from an exterior region that has much higher C_f fluctuation amplitudes and might be imagined to be exposed to freestream conditions. More of the outboard surface of the F-57 LDB-KE is exposed to freestream conditions than the Myring LDB. If the desired effect of the KE is to modify streamlines that have passed over the body, then the larger wake influence of the Myring body might be preferred. Because the KE is already immersed in a low-speed wake, the smaller increase in C_{DV} may also be both preferred and expected.

Figures 18a and 18b show U_z/U as a function of y/r of the Myring LDB with and without a KE similar to Fig. 10 for the F-57 LDB. As for the F-57, at all nonzero δ, the Myring-NKE and -KE profiles are very different, with much stronger net downwash at $\delta = 4$ and 6 deg for KE. The KE influence for the two bodies is compared for $\delta = 4$ deg in Fig. 19. The Myring LDB-KE has much larger positive and negative peaks in U_z, which nevertheless led to its having a larger $C_{L,\delta}$ (cf. Figs. 9a and 16a).

Figure 20 shows $L/D(\delta)$ for both LDBs. L/D is about three to four times higher for KE than NKE for both bodies. If L/D is a performance objective, then it is much better to have a deflector plate than to simply camber the body itself. At all δ, the Myring LDB has superior L/D, for either KE or NKE condition.

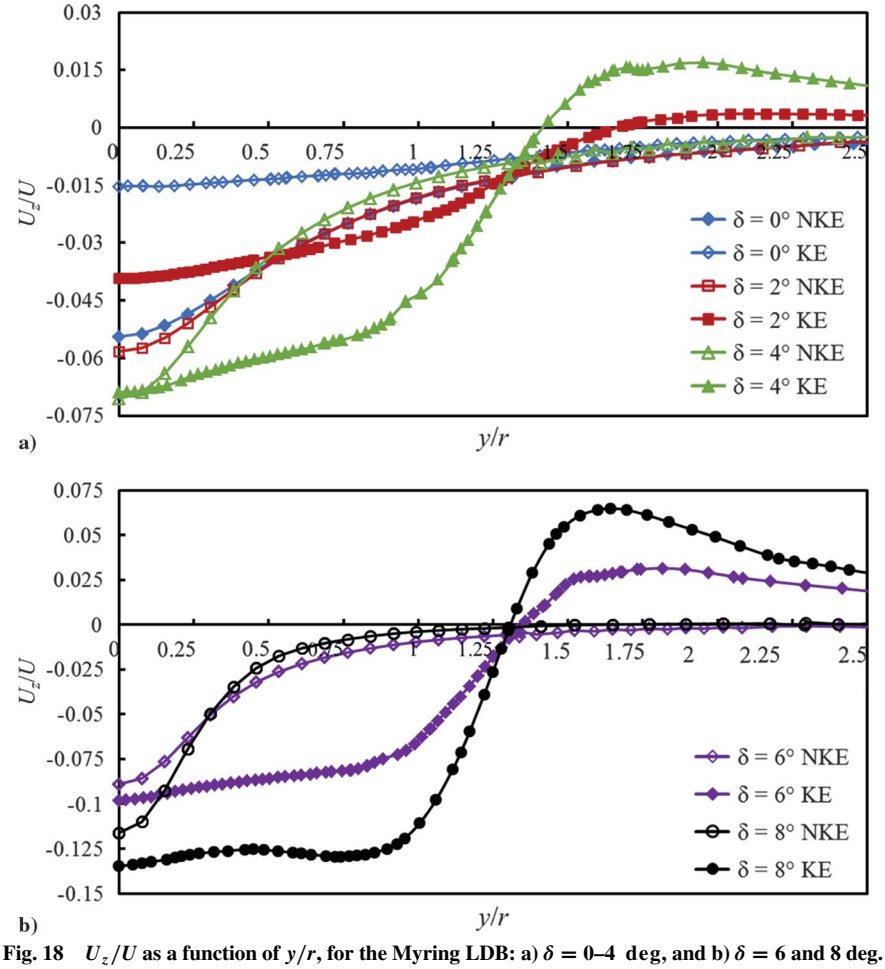

Fig. 18 U_z/U **as a function of** y/r**, for the Myring LDB: a)** $\delta = 0$**–4 deg, and b)** $\delta = 6$ **and 8 deg.**

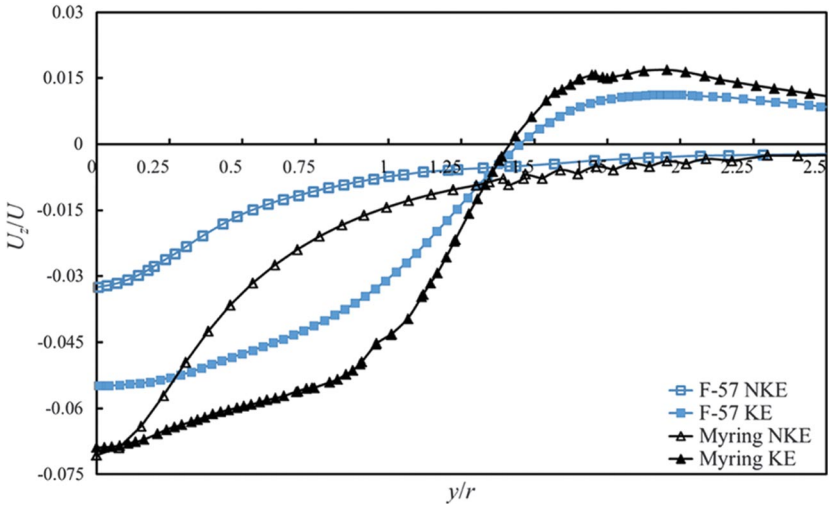

Fig. 19 Comparison of U_z/U as a function of y/r, with and without a KE, for the F-57 and Myring LDB at $\delta = 4$ deg.

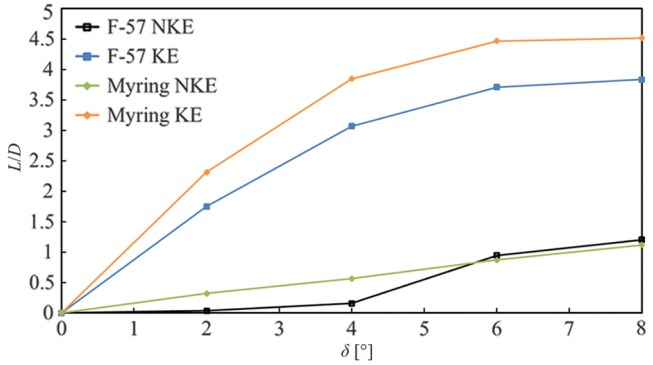

Fig. 20 Efficiency L/D for the F-57 and Myring's LDB with and without a KE at different δ.

V. Conclusions

RANS simulations were conducted for two low-drag bodies and compared with theoretical and experimental literature. The comparisons were close enough to encourage the subsequent testing of novel body-tail combinations, where the F-57 and Myring shapes were combined with a deflected tail plate (termed a Kutta edge, from its design objective to manipulate a trailing Kutta edge condition). The configurations were thus F-57 LDB (with and without KE) and Myring LDB (with and without KE). In both cases, the plate deflection was achieved by deflecting the entire aftbody, and so a deflection angle δ describes both plate and aftbody deflection.

Simple deflection of the aftbody provides camber and so predictably increases lift in all cases, even with no tail. This lift increase is greatly enhanced with the addition of the KE, and the average lift slope of the Myring LDB-KE is higher than that for F-57 LDB-KE. It appears that the width of the KE relative to the LDB geometry influences the overall efficiency of the LDB-KE configuration. The aftbody and tail geometry should be designed as a continuous unit and not in isolation, and it appears that an optimal arrangement could be found by locating the KE entirely within the bounds of the viscous wake. This maximizes the favorable manipulation of streamlines over the preceding body contours while minimizing the drag penalty of being exposed to the freestream.

Acknowledgments

The authors would like to thank the South African National Aerospace Center and Airbus for their financial support with this research project.

References

[1] Agenbag, D. S., Theron, N. J., and Huyssen, R. J., "Pitch Handling Qualities Investigation of the Tailless Gull-Wing Configuration," *Journal of Aircraft*, Vol. 46, No. 2, 2009, pp. 683–691. doi:10.2514/1.39755

[2] Young, A. D., "The Calculation of the Total and Skin Friction Drags on Bodies of Revolution at Zero Incidence," Air Ministry Rept. 1874, 1939.

[3] Carmichael, B. H., "Computer Study to Establish the Lower Limit of Length-to-Diameter Rates Advisable for Low-Drag Bodies," North American Aviation Rept. SID64-1938, Downey, CA, 1964.

[4] Carmichael, B. H., "Underwater Vehicle Drag Reduction Through Choice of Shape," *AIAA Second Propulsion Joint Specialist Conference*, AIAA Paper 1966-657, June 1966.

[5] Krauss, E. S., "Effect of Shapes of Conventional Fuselages and of Streamlined Bodies on Drag at Subsonic Speeds," *Zeitscrift fur flugwissenschaft und weltraumforschung*, Vol. 16, No. 12, Dec. 1968, pp. 429–438.

[6] Parsons, J. S., and Goodson, R. E., "Optimum Shaping of Axisymmetric Bodies for Minimum Drag in Incompressible Flow," Ph.D. Dissertation, Purdue Univ., West Lafayette, IN, 1972.

[7] Myring, D. F., "The Profile Drag of Bodies of Revolution in Subsonic Axisymmetric Flow," Royal Aircraft Establishment TR 72234, Farnborough, Hants, 1972.

[8] Myring, D. F., "A Theoretical Study of the Effects of Body Shape and Mach Number on the Drag Bodies of Revolution in Subcritical Axisymmetric Flow," Royal Aircraft Establishment TR 8100, Farnborough, Hants, 1981.

[9] Patel, V. C., and Lee, Y. T., "Thick Axisymmetric Turbulent Boundary Layer and Near Wake of a Low-Drag Body of Revolution," Iowa Inst. of Hydraulic Research, Univ. of Iowa Rept. 210, Iowa City, IA, 1977.

[10] Chappell, P. D., "Analysis of Axisymmetric Body Profile Drag Data at Zero Incidence Using Myring's Method," ESDU, Memorandum No. 28, ESDU International, London, 1978.

[11] Pinebrook, W. E., and Dalton, C., "Drag Minimization on a Body of Revolution Through Evolution," *Computer Methods in Applied Mechanics and Engineering*, Vol. 39, No. 2, 1983, pp. 179–197. doi:10.1016/0045-7825(83)90020-8

[12] Lutz, T., and Wagner, S., "Drag Reduction and Shape Optimization of Airship," *Journal of Aircraft*, Vol. 35, No. 3, 1998, pp. 345–351. doi:10.2514/2.2313

[13] Li, Y., Nahon, M., and Sharf, I., "Airship Dynamics Modeling: A Literature Review," *Progress in Aerospace Science*, Vol. 47, No. 3, 2011, pp. 217–239. doi:10.1016/j.paerosci.2010.10.001

[14] Smith, A. M. O., Stokes, R. T., and Lee, R. S., "Optimum Tail Shapes for Bodies of Revolution," *Journal of Hydronautics*, Vol. 15, Nos. 1–4, 1981, pp. 67–73. doi:10.2514/3.48186

[15] Huyssen, R. J., Spedding, G. R., Mathews, E. H., and Liebenberg, L., "Wing–Body Circulation Control by Means of a Fuselage Trailing

Edge," *Journal of Aircraft*, Vol. 49, No. 5, 2012, pp. 1279–1289. doi:10.2514/1.C031543

[16] Davis, T. W., and Spedding, G. R., "Lift and Drag Measurements of a Gull-Wing Configuration Aircraft," *53rd AIAA Aerospace Sciences Meeting*, AIAA Paper 2014-0027, Jan. 2014.

[17] "Star-CCM+ User's Guide, Version 8.06," CD-Adapco, Melville, NY, 2013.

[18] "Standard for Verification and Validation in Computational Fluid Dynamics and Heat Transfer," American Society of Mechanical Engineers, V&V 20, New York, 2009.

[19] Menter, F. R., "Two-Equation Eddy-Viscosity Turbulence Models for Engineering Applications," *AIAA Journal*, Vol. 32, No. 8, 1994, pp. 1598–1605. doi:10.2514/3.12149

[20] Menter, F. R., "Improved Two-Equation k–ω. Turbulence Models for Aerodynamic Flows," NASA TM-103975, 1992.

[21] Menter, F. R., Langtry, R. B., Likki, S. R., Suzen, Y. B., Huang, P. G., and Volker, S., "A Correlation-Based Transition Model Using Local Variables Part 1—Model Formulation," *Journal of Turbomach*, Vol. 128, No. 3, 2004, pp. 413–422.